Check for updates

Functional optoretinography: concurrent OCT monitoring of intrinsic signal amplitude and phase dynamics in human photoreceptors

GUANGYING MA,[1] ![iD] TAEYOON SON,[1] TAE-HOON KIM,[1] ![iD] AND XINCHENG YAO[1,2,*] ![iD]

[1]*Department of Bioengineering, University of Illinois at Chicago, Chicago, IL 60607, USA*
[2]*Department of Ophthalmology and Visual Sciences, University of Illinois at Chicago, Chicago, IL 60612, USA*
[*]*xcy@uic.edu*

Abstract: Intrinsic optical signal (IOS) imaging promises a noninvasive method for objective assessment of retinal function. This study demonstrates concurrent optical coherence tomography (OCT) of amplitude-IOS and phase-IOS changes in human photoreceptors. A new procedure for differential-phase-mapping (DPM) is validated to enable depth-resolved phase-IOS imaging. Dynamic OCT revealed rapid amplitude-IOS and phase-IOS changes, which occur almost right away after the stimulus onset. These IOS changes were predominantly observed within the photoreceptor outer segment (OS), particularly two boundaries connecting to the inner segment and retinal pigment epithelium. The comparative analysis supports that both amplitude-IOS and phase-IOS attribute to transient OS morphological change associated with phototransduction activation in retinal photoreceptors. A simulation modeling is proposed to discuss the relationship between the photoreceptor OS length and phase-IOS changes.

1. Introduction

Retinal photoreceptors are responsible for capturing photons and converting light energy to bioelectric signals for visual information processing. Photoreceptor dysfunctions have been frequently observed in eye diseases, such as age-related macular degeneration (AMD) [1–3], retinitis pigmentosa (RP) [4,5], and diabetic retinopathy (DR) [6,7]. Therefore, functional assessment of retinal photoreceptors is essential for clinical screening, diagnosis, and treatment assessment of eye diseases. Electrophysiological measurements, such as electroretinography (ERG), can provide an objective assessment of retinal function. The ERG a-wave can be used for functional evaluation of photoreceptor physiology. However, the spatial resolution of ERG measurement is limited, and the ERG a-wave can also be affected by inner retinal neural activity.

Functional intrinsic optical signal (IOS) imaging [8], also termed as optophysiology [9], optoretinogram [10–12], or optoretinography (ORG) [12–14], promises a high resolution alternative to ERG for functional measurement of retinal physiology. The terminology ORG is analog to ERG. While the ERG is recording stimulus-evoked electrical dynamics for electrophysiological measurement of retinal neural activation, the ORG is mapping stimulus-evoked IOS changes for pathophysiological measurement of retinal neural activation. For retinal IOS imaging, a near-infrared (NIR) light is typically used for recording IOS changes, and visible light is employed for retinal stimulation [15]. By providing excellent axial imaging capability, optical coherence tomography (OCT) provides a unique imaging modality to map IOSs at individual layers. Functional OCT has been used for IOS imaging studies of both animal [14,16–18] and human [8,10,12,13,19] retinas. Depth-resolved OCT revealed a rapid IOS at the photoreceptor outer segment (OS) known to be the center of phototransduction [20]. Further development of the functional OCT promises objective ORG assessment of retinal photoreceptors.

In principle, OCT can provide both amplitude and phase information. Dynamic OCT amplitude measurement was first used for functional IOS imaging of retinal activation [21–23]. Recently, OCT phase measurement was also explored for monitoring the OS changes due to retinal stimulation [12,19,24]. However, there is no reported study to characterize the relationship between the amplitude-IOS and phase-IOS changes directly. Previous phase-IOS studies focused on the relative phase difference between two retinal depths [12,19,24,25]. However, given the complexity of retinal structure, particularly the difficulty of identifying a specific location such as photoreceptor tip of individual photoreceptors, depth-resolved phase mapping at high resolution is desirable for comparative amplitude-IOS and phase-IOS investigation. Moreover, the phototransduction change at the OS and mitochondria metabolism at the inner segment (IS) may also change the optical property of these regions locally [26], making the interpretation of the phase change between two separate layers complicated. In this article, we report a new procedure for dynamic differential-phase-mapping (DPM) to enable concurrent amplitude-IOS and phase-IOS monitoring with a spatial resolution at the sub OS level.

2.　Materials and methods

2.1.　Experimental setup

A custom-designed OCT was developed for retinal IOS imaging [8]. The same instrument and experimental protocol were used for this study. Briefly, a NIR broadband superluminescent diode (D-840-HP-I, Superlum, Cork, Ireland, λ_{center} = 840 nm, $\Delta\lambda$ = 100 nm) was used as a light source. The illumination power was ~600 μW on the cornea. The estimated optical resolutions in lateral and axial directions were 12 and 3 μm, respectively. A dim red light was used as a fixation target to minimize voluntary eye movements. A white LED was used as the retinal stimulator. The stimulus strength was 1.2×10^4 photons·μm^{-2}·ms^{-1}. Two OCT imaging speed modes were used to characterize IOS changes in the retina. For images in Fig. 1 and Fig. 2, the imaging speed was 100 B-scans per second with each B-scan containing 500 A-lines covering a 2.5 mm retina. For the experiment in Fig. 3(B), the imaging speed was 1000 B-scans per second with each B-scan containing 50 A-lines covering a 0.25 mm retina.

2.2.　Human subject and imaging

This study was approved by the Institutional Review Board of the University of Illinois at Chicago and followed the ethical standards stated in the Declaration of Helsinki. Each subject provided informed consent prior to participation in the research. Before IOS imaging, the subject was dark adapted at least for a half-hour.

2.3.　Data analysis

2.3.1.　Differential phase processing

Figure 1(A) illustrates the flow chart of OCT image construction and DPM processing. As shown in Fig. 1(A), the digital dispersion compensation was applied to the raw OCT spectrogram, and then five times zero-padding was implemented before the fast Fourier transform (FFT). A complex matrix, including both light amplitude (Fig. 1(B)) and phase (Fig. 1(C)) information, is available for each OCT dataset. For Fig. 1(B) and Fig. 1(C), the pixel resolution in the axial and lateral directions were 0.36 μm and 5 μm, respectively. Phase unwrapping in the axial direction was implemented on Fig. 1(C) to produce Fig. 1(D), followed by differential phase processing (Fig. 1(E)), i.e., the phase difference among two adjacent pixels in the axial direction sequentially. As shown in Fig. 1(E), the DPM can reasonably reflect the layer structures in Fig. 1(B). Figure 1(F1) and 1(F2) show enlarged illustrations of the yellow windows in Fig. 1(B) and Fig. 1(E). In principle, DPM corresponds to local phase dynamics in the axial direction. If the two adjacent pixels (pixels m and m-1 in Fig. 1(G1)) in axial direction correspond to one
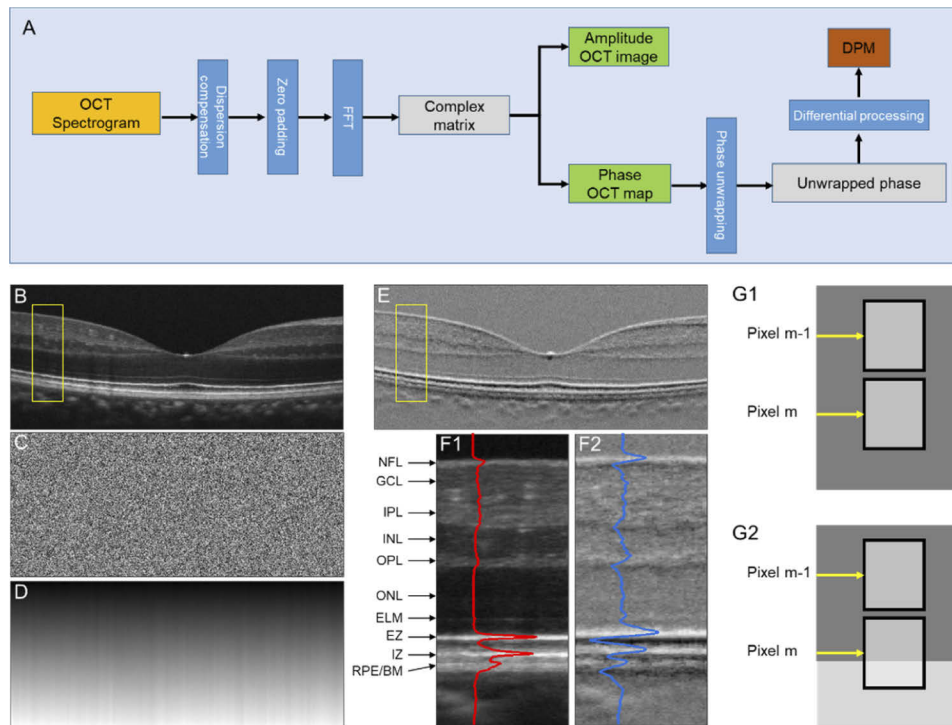
Fig. 1. (A) A flow chart of amplitude OCT and DPM processing. Representative OCT amplitude image (B), corresponding phase map (C), unwrapped phase map (D), and DPM (E). (F) Flattened amplitude (F1) and DPM (F2) images corresponding to the yellow rectangular areas in (B) and (E). The blue and red curves show the waveform profiles of the amplitude image and DPM. NFL, nerve fiber layer; GCL, ganglion cell layer; IPL, inner plexiform layer; INL inner nuclear layer; OPL, outer plexiform layer; ONL, outer nuclear layer; ELM, external limiting membrane; EZ, ellipsoid zone; IZ, interdigitation zone; RPE, retinal pigment epithelium; BM, Bruch's membrane. (G) Schematic diagram of differential phase interpretation.

even background, i.e., the regions with even distributed scatters, the corresponding differential phase value will be $4\pi nL/\lambda$, where L is the pixel size, n is the average refractive index, and λ is the center wavelength of the OCT light source. The phase value $4\pi nL/\lambda$ here considers the light double passing property for reflectance imaging modality in OCT [27]. However, if one of the two adjacent pixels (pixels m and m-1 in Fig. 1(G2)) in axial direction covers one junction region (i.e., hypo- or hyper-reflective band), the corresponding differential phase value can be different from the value $4\pi nL/\lambda$. In other words, the overall background value in Fig. 1(E) is $4\pi nL/\lambda$, and individual pixel values are dependent on the local phase dynamics in the axial direction (Fig. 1(G)).

2.3.2.   OCT IOS processing

Before IOS processing, the bulk movement between B-scans was compensated by 2D image registration. To investigate the IOS of each retinal layer, B-scans were flattened by aligning the interdigitation zone (IZ) to a straight band. Amplitude-IOS and phase IOS were computed from amplitude images and DPM, respectively. Amplitude-IOS and phase-IOS active pixels are computed following the steps; we take amplitude-IOS as an example. 1) The background was computed by averaging all the frames recorded in the pre-stimulation time. The mean value and
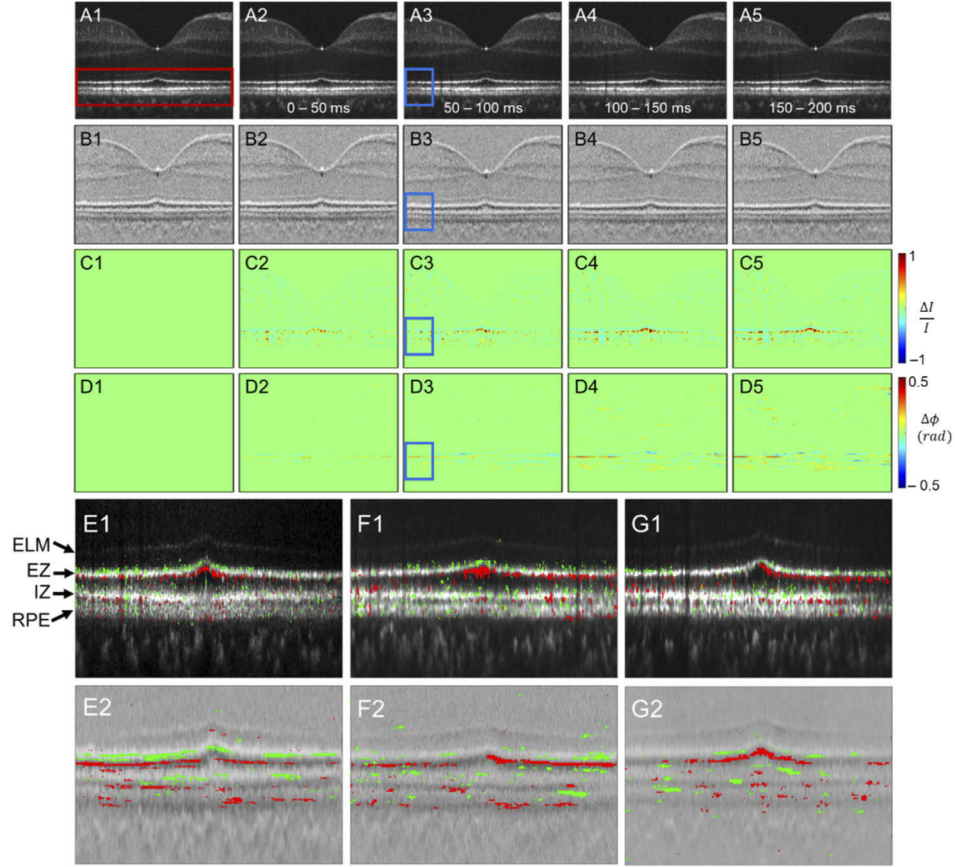
Fig. 2. The amplitude-IOS and phase-IOS distribution. (A) Amplitude image sequence. (B) DPM sequence. (C) Amplitude-IOS sequence. (D) Phase-IOS sequence. (E) The positive (red) and negative (green) amplitude-IOS (E1) and phase-IOS (E2) active pixel distribution. (F, G) IOS active pixel distribution for additional two human subjects.

the standard deviation of each pixel were defined as $\bar{I}_{pre}(x, y)$ and $\sigma(x, y)$. 2) The intensity of each pixel in the post-stimulation images was compared with the background. If the pixel intensity was larger than $\bar{I}_{pre}(x, y) + 3 \times \sigma(x, y)$ or smaller than $\bar{I}_{pre}(x, y) - 3 \times \sigma(x, y)$, the corresponding pixel value was reserved. 3) Consecutive rule was next applied to avoid random noise. If the IOS response at a specific pixel did not recur at least three times continuously, the response was ignored. The amplitude-IOS value is defined as the $\Delta I/I_{pre}$, meaning the amplitude change is divided by the background value. The phase IOS value is defined as $\Delta\phi$, meaning the phase change. The average amplitude-IOS curves were computed by average all the IOS between the external limiting membrane (ELM) and retinal pigment epithelium (RPE) layer. Average optical path length change (ΔOPL) is computed by two steps; first, we calculated the relative phase change $\Delta\phi$ between the ELM and RPE layers by summing the DPM value between these two layers, then ΔOPL is computed from the $\Delta\phi$ and central wavelength (λ) according to the following equation. ΔOPL for |phase-IOS| was computed from $|\Delta\phi|$, following a similar procedure.

$$\Delta OPL = \frac{\Delta\phi \times \lambda}{4\pi} \tag{1}$$
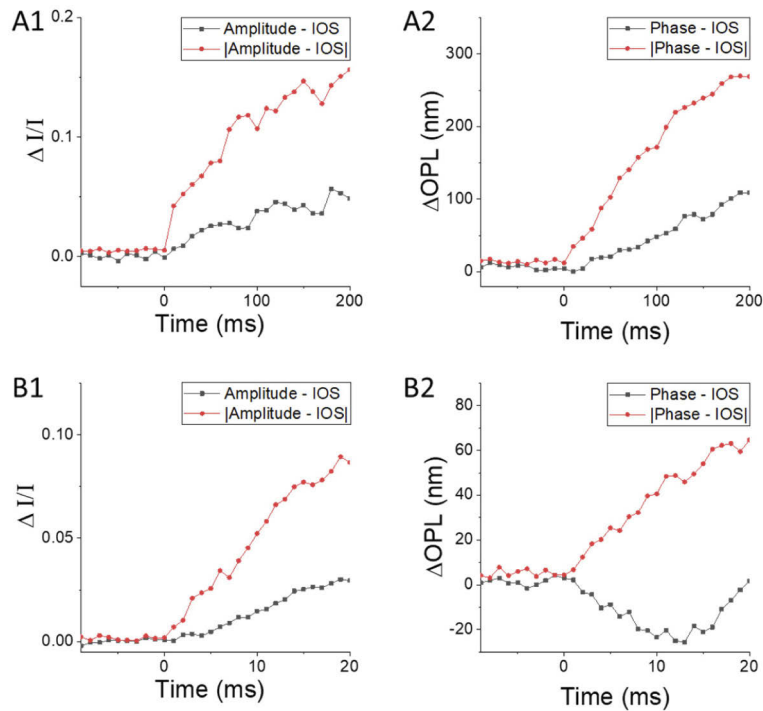
Fig. 3. Amplitude-IOS and phase-IOS at different time courses correspond to Fig. 2. (A) Amplitude-IOS (A1) and phase-IOS (A2) with 10 ms temporal resolution. (B) Amplitude-IOS (A1) and phase-IOS (A2) with 1 ms temporal resolution.

3. Results

Figure 2 shows representative OCT-IOS imaging. Both amplitude-IOS and phase-IOS were observed right after the stimulus onset, predominantly in the outer retina. As shown in Fig. 2(C) and Fig. 2(D), both positive and negative changes were observed in amplitude-IOS and phase-IOS maps. The positive and negative amplitude-IOSs reflect increased and decreased reflectance intensity compared to the pre-stimulus baseline. The positive and negative phase-IOSs reflect increased and decreased phase difference between adjacent pixels in the axial direction.

Figure 2(E1) and Fig. 2(E2) show the enlarged outer retina region (red window in Fig. 2(A1)) mapped with positive (red) and negative (green) active IOS pixels. We observed that the IOS changes were predominantly within the outer retina, i.e., the region between the ELM and RPE. Both positive and negative IOSs were consistently observed in the amplitude-IOS and phase-IOS maps. This is the first-time observation of the mixed positive and negative phase-IOS changes, reflecting transient changes of local scatters/boundaries in the axial direction. To verify the reliability, IOS distributions in additional two human subjects are provided in Fig. 2(F) and Fig. 2(G).

For quantitative assessment of the effect of the spatial resolution on IOS sensitivity, Fig. 3 shows a comparative illustration of amplitude-IOS/phase-IOS and |amplitude-IOS|/|phase-IOS| averages, corresponding to the image sequence in Fig. 2(C)/Fig. 2(D). |Amplitude-IOS|/|phase-IOS| refers to the absolute value of each pixel by converting negative IOS to positive IOS for averaging. As the positive and negative IOS signals were mixed (Fig. 2), the direct averaging of IOS magnitudes was smaller than the absolute value assessments (Fig. 3(A)). As shown in Fig. 3(A), both amplitude-IOS and phase-IOS occurred almost right away after the onset of

retinal stimulation. The imaging speed for the experiment in Fig. 3(A) was 100 frames/s, i.e., 10 ms temporal resolution. In order to verify the onset time of the IOS changes, the result of another experiment with imaging speed at 1000 frames/s was illustrated in Fig. 3(B). Both amplitude-IOS and phase-IOS were confirmed to occur almost right away after the retinal stimulation, consistent with previous studies [8,12,18]. For the phase-IOS changes at the outer retina, they were converted to an optical path length change $\Delta OPL = \Delta\phi\lambda/4\pi$ in Fig. 3(A2) and Fig. 3(B2), for easy comparison to early studies [12,19,24]. As shown in Fig. 3(B2), the ΔOPL shows a negative response first, with the time-to-valley between 10-15 ms, followed by a positive-going response. This observation is consistent with the previous study of phase change at photoreceptor OS [12,19,24].

In order to better investigate the spatiotemporal distribution of IOS changes, Fig. 4(A), Fig. 4(B), Fig. 4(C), and Fig. 4(D) show enlarged illustrations of the blue window regions in Fig. 2(A3), Fig. 2(B3), Fig. 2(C3), and Fig. 2(D3), respectively. As shown in Fig. 2 and Fig. 4, the IOS changes, particularly the phase-IOS responses, were predominantly at the boundary regions of hypo- and hyper-reflective bands, which suggests that the boundary-sensitive phase-IOS responses may reflect stimulus-evoked OS change [28]. To verify the possible outer retina changes, the average reflectance amplitude (Fig. 4(E1)) and differential phase (Fig. 4(E2)) profiles of the retinal region shown in Fig. 4(A) and Fig. 4(B) are illustrated. Different colors reflect the OCT profiles corresponding to 5-time points, i.e., 0 ms, 50 ms, 100 ms, 150 ms, and 200 ms after the onset of retinal stimulation. In Fig. 4(E1), the ELM location and amplitude were overserved to be stable. On the contrary, the ellipsoid zone (EZ), IZ, and RPE peak values showed dynamic changes, which can be reflected by the amplitude-IOS changes in Fig. 4(C). The EZ and OS amplitude change is consistent with previous publications [16]. Corresponding differential-phase peak value and location changes, particularly at the V_1 and V_2, were also observed in Fig. 4(E2). The observed V_1 and V_2 dynamics can be reasonably correlated to the observed phase-IOS changes nearby the EZ and IZ region in Fig. 4(D).
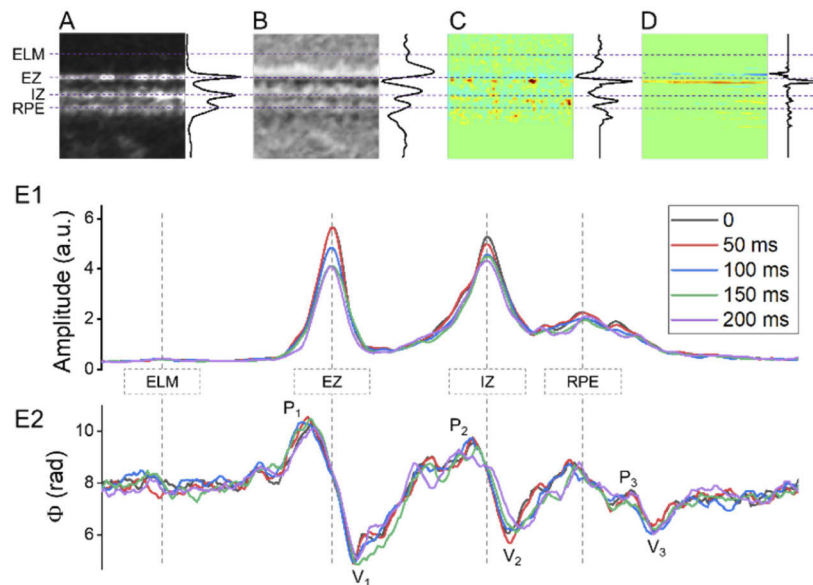

Fig. 4. A, B, C, and D are enlarged illustrations of the blue window regions in Fig. 2(A3), Fig. 2(B3), Fig. 2(C3), and Fig. 2(D3), respectively. The average signal of each horizontal line is illustrated at the right of each image. (E) OCT reflectance amplitude (E1) and phase (E2) profile dynamics corresponding to the retinal region in A and B.

4.   Discussion

In summary, a new procedure for DPM analysis was developed to enable robust phase-IOS mapping. The phase wrapping and stabilization issues are known to affect the phase-resolved measurement [19]. We applied a zero-padding procedure to increase the sampling rate before the reconstruction, which ensured an efficient phase unwrapping (Fig. 1(D)). After unwrapping, a differential procedure was applied to extract the relative phase of each pixel, compared to the adjacent location in the axial direction (Fig. 1(E)). The differential procedure can naturally reject the effect of the phase drift caused by bulk movement and can also exclude the possible accumulated phase noise from each pixel along the A-line direction. The DPM enabled comparative OCT amplitude-IOS and phase-IOS mapping at high resolution (Fig. 2). Both amplitude-IOS and phase-IOS responses, which occur almost right away after the stimulus onset, were primarily observed within the OS, the center of phototransduction. Mixed positive and negative IOS changes were consistently observed in both amplitude-IOS and phase-IOS maps, indicating the importance of spatial resolution for sensitive IOS recording.

The high-resolution DPM differentiates this work from previous OCT phase-sensitive measurements, which only measured the relative phase change of two separate layers [12,19,24,25]. In principle, the relative phase measurement of two separate layers, such as the IS/OS boundary relative to the OS tip, can be used to quantify the OS length change evoked by visible light stimulation. However, reliable identification of these IS/OS and photoreceptor tip boundaries can be challenging, particularly unavoidable band variance in the lateral direction. Moreover, an accurate interpretation of the increased/decreased phase value is complicated. As shown in Fig. 1(G), the relative phase value of two pixels corresponding to two retinal depths can be sensitive to the dynamic change of local scatters or tissue boundaries.

For better understanding the complexity of the phase interpretation, Fig. 5 illustrates simulated OS length change (Fig. 5(A)) and corresponding OCT phase change (Fig. 5(B)). In Fig. 5(A), the OCT pixel 0, which corresponds to a specific retinal depth such as the IS/OS junction, has a phase value at ϕ; the relative phase value of pixel m, which corresponds to another retinal depth such as OS tip, can be estimated within the range between $\phi + (4\pi nmL - 2\pi nL)/\lambda$ and $\phi + (4\pi nmL + 2\pi nL)/\lambda$, where L is the axial length of a pixel, n is the average refractive index, and λ is the center wavelength of the OCT light source. The actual phase value of pixel m is dependent on the scatter/boundary location within the sampling volume. At time t_0, if we assume the sampling volume of the pixel m corresponds to one evenly hypo-reflective region, the phase value can be reasonably estimated at $\theta_0 = \phi + 4\pi nmL/\lambda$. At time t_1, t_2, and t_3, if we assume: 1) the OS tip right reach the bottom, middle, and top regions of the sampling region, respectively; and 2) the OS tip corresponds to a hyper-reflective band to dominate the signal detected by pixel m, the phase value can be reasonably estimated at $\theta_1 = \phi + (4\pi nmL + 2\pi nL)/\lambda$, $\theta_2 = \phi + 4\pi nmL/\lambda$, $\theta_3 = \phi + (4\pi nmL - 2\pi nL)/\lambda$, respectively. At time t_4, the OS tip right above the sampling region, corresponding to one evenly hyper-reflective region, the phase value can be estimated at $\theta_4 = \phi + 4\pi nmL/\lambda$, i.e., equivalent to a scatter at the middle of the sampling volume pixel m. The relative phase values of the pixel m, relative to the stationary pixel 0, will be $\Delta\theta_0 = 4\pi nmL/\lambda$, $\Delta\theta_1 = (4\pi nmL + 2\pi nL)/\lambda$, $\Delta\theta_2 = 4\pi nmL/\lambda$, $\Delta\theta_3 = (4\pi nmL - 2\pi nL)/\lambda$, and $\Delta\theta_4 = 4\pi nmL/\lambda$. Solely using the relative phase value as in previous publications [12,19,24,25], the interpretation of transient OS length or optical pathlength changes at t_0-t_1 and t_3-t_4 can be difficult. As shown in Fig. 5, the simulated OS length is gradually reduced, i.e., unidirectional changes from time t_0 to t_4. However, corresponding phase changes show a complicated non-unidirectional pattern waveform. Moreover, the phototransduction change at the OS and mitochondria metabolism at inner segment IS may also change the optical properties, such as the reflective index or morphological structures of retinal regions locally, making the quantitative interpretation of the phase change more complicated.
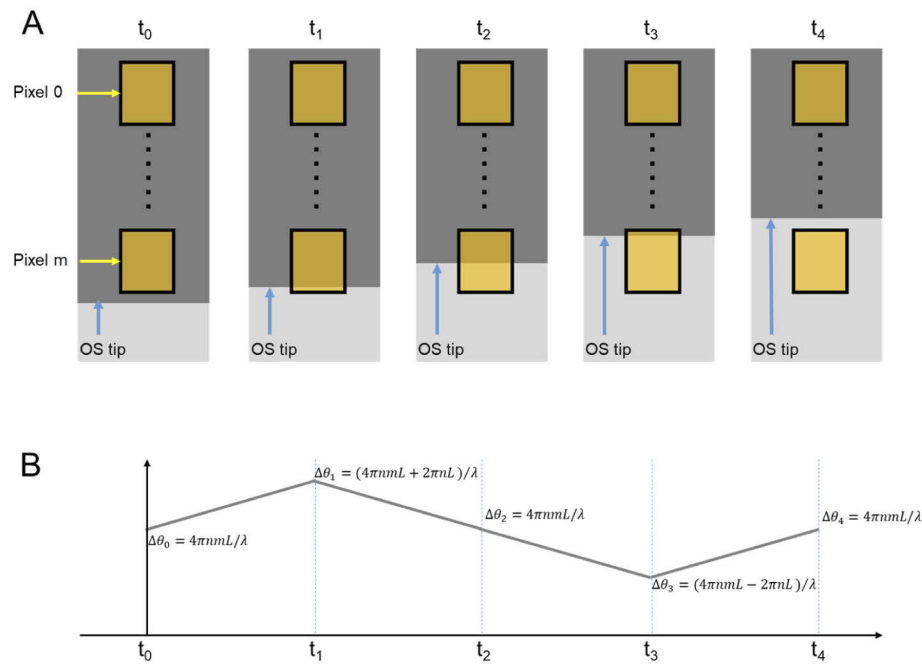
Fig. 5. Simulation of the relationship between OS length (A) and OCT phase (B) changes.

5.   Conclusion

In conclusion, dynamic DPM provides a simple but robust strategy to monitor the transient phase-IOS changes at the photoreceptor OS. Unambiguous phase changes were observed at the OS boundaries to both IS and RPE sides. The comparative analysis supports that both amplitude-IOS and phase-IOS maps contribute to transient OS morphological change correlated with phototransduction activation in retinal photoreceptors. In principle, the tension force, due to OS shrinkage or elongation due to phototransduction activation, can affect the phase value changes at both the IS and RPE sides. However, direct conversion of a positive/negative phase value to increased/decreased OS length change is not warranted due to the complexity of phase relationship to the scatter distribution relative to the center of the sampling volume of one OCT pixel. Further development of a strategy for quantitative OCT analysis of OS length change is required.

Disclosures.   The authors declare that there are no conflicts of interest related to this article.

References

1. C. A. Curcio, N. E. Medeiros, and C. L. Millican, "Photoreceptor loss in age-related macular degeneration," Invest Ophthalmol. Vis. Sci. **37**(7), 1236–1249 (1996).
2. S. Yang, C. Zuo, H. Xiao, L. Mi, G. Luo, X. Xu, and X. Liu, "Photoreceptor dysfunction in early and intermediate age-related macular degeneration assessed with mfERG and spectral domain OCT," Doc. Ophthalmol. **132**(1), 17–26 (2016).
3. G. R. Jackson, C. Owsley, and C. A. Curcio, "Photoreceptor degeneration and dysfunction in aging and age-related maculopathy," Ageing Res. Rev. **1**(3), 381–396 (2002).
4. E. L. Berson, P. Gouras, and R. D. Gunkel, "Rod responses in retinitis pigmentosa, dominantly inherited," Arch. Ophthalmol. **80**(1), 58–67 (1968).
5. E. L. Berson and E. B. Goldstein, "Early receptor potential in dominantly inherited retinitis pigmentosa," Arch. Ophthalmol. **83**(4), 412–420 (1970).

6. K. Holopigian, V. C. Greenstein, W. Seiple, D. C. Hood, and R. E. Carr, "Evidence for photoreceptor changes in patients with diabetic retinopathy," Invest Ophthalmol. Vis. Sci. **38**(11), 2355–2365 (1997).

7. J. J. McAnany and J. C. Park, "Cone photoreceptor dysfunction in early-stage diabetic retinopathy: association between the activation phase of cone phototransduction and the flicker electroretinogram," Invest. Ophthalmol. Visual Sci. **60**(1), 64–72 (2019).

8. T. Son, T. H. Kim, G. Ma, H. Kim, and X. Yao, "Functional intrinsic optical signal imaging for objective optoretinography of human photoreceptors," Exp. Biol. Med. (Maywood) **246**(6), 639–643 (2021).

9. K. Bizheva, R. Pflug, B. Hermann, B. Povazay, H. Sattmann, P. Qiu, E. Anger, H. Reitsamer, S. Popov, J. R. Taylor, A. Unterhuber, P. Ahnelt, and W. Drexler, "Optophysiology: depth-resolved probing of retinal physiology with functional ultrahigh-resolution optical coherence tomography," Proc. Natl. Acad. Sci. U. S. A. **103**(13), 5066–5071 (2006).

10. M. Azimipour, D. Valente, K. V. Vienola, J. S. Werner, R. J. Zawadzki, and R. S. Jonnal, "Optoretinogram: optical measurement of human cone and rod photoreceptor responses to light," Opt. Lett. **45**(17), 4658–4661 (2020).

11. P. Zhang, B. Shibata, G. Peinado, R. J. Zawadzki, P. FitzGerald, and E. N. Pugh Jr., "Measurement of diurnal variation in rod outer segment length in vivo in mice with the OCT optoretinogram," Invest. Ophthalmol. Visual Sci. **61**(3), 9 (2020).

12. V. P. Pandiyan, A. Maloney-Bertelli, J. A. Kuchenbecker, K. C. Boyle, T. Ling, Z. C. Chen, B. H. Park, A. Roorda, D. Palanker, and R. Sabesan, "The optoretinogram reveals the primary steps of phototransduction in the living human eye," Sci. Adv. **6**(37), eabc1124 (2020).

13. R. F. Cooper, D. H. Brainard, and J. I. W. Morgan, "Optoretinography of individual human cone photoreceptors," Opt. Express **28**(26), 39326–39339 (2020).

14. T.-H. Kim, B. Wang, Y. Lu, T. Son, and X. Yao, "Functional optical coherence tomography enables in vivo optoretinography of photoreceptor dysfunction due to retinal degeneration," Biomed. Opt. Express **11**(9), 5306–5320 (2020).

15. X. Yao and B. Wang, "Intrinsic optical signal imaging of retinal physiology: a review," J. Biomed. Opt. **20**(9), 090901 (2015).

16. W. Suzuki, K. Tsunoda, G. Hanazono, and M. Tanifuji, "Stimulus-induced changes of reflectivity detected by optical coherence tomography in macaque retina," Invest. Ophthalmol. Visual Sci. **54**, 6345–6354 (2013).

17. P. Zhang, R. J. Zawadzki, M. Goswami, P. T. Nguyen, V. Yarov-Yarovoy, M. E. Burns, and E. N. Pugh, "In vivo optophysiology reveals that G-protein activation triggers osmotic swelling and increased light scattering of rod photoreceptors," Proc. Natl. Acad. Sci. U. S. A. **114**(14), E2937–E2946 (2017).

18. B. Wang, Y. Lu, and X. Yao, "In vivo optical coherence tomography of stimulus-evoked intrinsic optical signals in mouse retinas," J. Biomed. Opt. **21**(9), 096010 (2016).

19. D. Hillmann, H. Spahr, C. Pfaffle, H. Sudkamp, G. Franke, and G. Huttmann, "In vivo optical imaging of physiological responses to photostimulation in human photoreceptors," Proc. Natl. Acad. Sci. U. S. A. **113**(46), 13138–13143 (2016).

20. X. Yao and T. H. Kim, "Fast intrinsic optical signal correlates with activation phase of phototransduction in retinal photoreceptors," Exp. Biol. Med. (Maywood) **245**(13), 1087–1095 (2020).

21. X. Yao, A. Yamauchi, B. Perry, and J. S. George, "Rapid optical coherence tomography and recording functional scattering changes from activated frog retina," Appl. Opt. **44**(11), 2019–2023 (2005).

22. X. Yao and J. S. George, "Dynamic neuroimaging of retinal light responses using fast intrinsic optical signals," NeuroImage **33**(3), 898–906 (2006).

23. Q. Zhang, R. Lu, B. Wang, J. D. Messinger, C. A. Curcio, and X. Yao, "Functional optical coherence tomography enables in vivo physiological assessment of retinal rod and cone photoreceptors," Sci. Rep. **5**(1), 9595 (2015).

24. F. Zhang, K. Kurokawa, A. Lassoued, J. A. Crowell, and D. T. Miller, "Cone photoreceptor classification in the living human eye from photostimulation-induced phase dynamics," Proc. Natl. Acad. Sci. U. S. A. **116**(16), 7951–7956 (2019).

25. C. Pfäffle, H. Spahr, L. Kutzner, S. Burhan, F. Hilge, Y. Miura, G. Hüttmann, and D. Hillmann, "Simultaneous functional imaging of neuronal and photoreceptor layers in living human retina," Opt. Lett. **44**(23), 5671–5674 (2019).

26. G. Ma, T. Son, T. H. Kim, and X. Yao, "In vivo optoretinography of phototransduction activation and energy metabolism in retinal photoreceptors," J. Biophotonics **2021**, e202000462 (2021).

27. A. Zhang, Q. Zhang, C.-L. Chen, and R. K. Wang, "Methods and algorithms for optical coherence tomography-based angiography: a review and comparison," J. Biomed. Opt. **20**(10), 100901 (2015).

28. Y. Lu, J. Benedetti, and X. Yao, "Light-induced length shrinkage of rod photoreceptor outer segments," Trans. Vis. Sci. Tech. **7**(6), 29 (2018).